KRONOS FUSION ENERGY

PAPER 2.84 · THE KRONOS 2026 SERIES

The Plasma Diagnostic Suite and Real-Time State Estimation for a Compact Spherical-Tokamak Breeder: Magnetics, Thomson, Interferometry, and Bolometry Fused by a Graph-Neural-Network Reconstructor

An autonomous controller can act only on the state it can see, and in a compact spherical tokamak the state must be produced faster than the plant evolves, from a diagnostic set...

Read it live — 3-D model · physics validator · film series

BY P I FORD

2026 · EDITORIAL EDITION

THE OFFICIAL RECORD

What this document is, and how to read its numbers

This is a combined editorial. It gathers, in one volume, the two design studies Kronos Fusion Energy released in 2026 — a compact spherical-tokamak tritium/helium-3 breeder and a deuterium–helium-3 tandem-mirror generator — together with the intellectual-property estate, the people, and, in the internal edition, the full commercial case. The scientific text is the same text that appears in the arXiv preprints and the journal submissions; the editorial adds the apparatus a reader needs to hold the whole program at once, and nothing in the physics is altered to fit it.

THE HONESTY STANCE IS THE ASSET

Every headline quantity carries an **evidence class** — DERIVED RECOMPUTED MEASURED REQUIREMENT — and, where a number is a modelled extrapolation rather than a demonstrated value, it is labelled as such and its downside is shown next to it. Several quantities in the underlying corpus moved after first publication; where a value has been withdrawn or restated, the record says so plainly. This is deliberate: a diligence team will find the load-bearing assumptions, so the document surfaces them first.

TWO EDITIONS

This volume is issued in two editions. The **public edition** (light) carries the physics and the design only — no dollar, price, or per-kilogram figure appears anywhere in it. The **internal edition** (dark) adds the economics, the funding architecture, and the defense-commercial analysis, and is marked *Confidential* accordingly; it is not for public distribution. Where the commercial case rests on a modelled assumption rather than a demonstrated one, it is labelled as such and its downside is shown alongside it, on the same terms as the physics.

TITLE	The Kronos Fleet — Hyperion · Aegis · MetroVolt: A Combined Design & Commercialization Study
AUTHOR	Priyanca Ford, Founder & CEO, on behalf of Kronos Fusion Energy
EDITION	2026 Combined Editorial · first issue
COMPANION WORKS	The five-paper arXiv drop — (1) Breeder, (2) Burner, (3) REBCO magnet & tape, (4) Direct Energy Conversion, (5) AI/ML/Quantum control — with matching numbered Zenodo deposits, plus the IOP journal and IAEA-FEC submissions. Patents were filed before the drop.
NAMING	Hyperion = the breeder; Aegis (defense) and MetroVolt (data-center) = one generator in two housings. Internal mode letters (D1, L) do not appear on public surfaces.
STATUS	Conceptual design & simulation study. Nothing herein is a construction commitment.

HOW TO READ THIS VOLUME

The fleet at a glance, and the way its numbers are marked

This volume opens with *Orientation*, presents the five research papers as a bound sequence, and closes with the *Apparatus*. *Foundations* sets out the three general results both machines rest on. *Paper One* is the Hyperion breeder; *Paper Two* the Aegis / MetroVolt generator; *Papers Three, Four and Five* are the enabling science — high-field REBCO magnets and tape, direct energy conversion, and the AI / ML / quantum control stack. A *Digital Twin & 3-D Model* part follows, then the *Environmental* profile. The *Economics* and levelized cost and the *Business Case* and diligence record appear in the internal edition only; the *Simulations* proof record and the Apparatus — patent portfolio, team, limitations, and sources — close both editions.

THE FLEET AT A GLANCE

	HYPERION	AEGIS	METROVOLT
Role	Strategic-isotope foundry	Defense installation power	Campus power
Machine	**Spherical tokamak**	**Tandem mirror**	**Tandem mirror**
Fuel	Deuterium–tritium	Deuterium–helium-3	Deuterium–helium-3
Delivers	Tritium · ^{3}He · 14 MeV n	Resilient installation power	Firm campus power
Physics bar	**Fusion gain only**	Closure (gates named)	Closure + lunar ^{3}He
In the fleet	Breeds the fuel	Proves the generator	Commercial destination

HOW THE NUMBERS ARE MARKED

Every headline quantity carries an evidence class — DERIVED from first principles, RECOMPUTED from raw data, MEASURED in hardware, or a REQUIREMENT yet to be met. Financial figures carry a case label and are confined to the internal (confidential) edition. Values that moved after first publication are shown as withdrawn or restated rather than quietly changed. A capability you can evaluate is one whose limits are on the page.

ABSTRACT

The Plasma Diagnostic Suite and Real-Time State Estimation for a Compact Spherical-Tokamak Breeder: Magnetics, Thomson, Interferometry, and Bolometry Fused by a Graph-Neural-Network Reconstructor

An autonomous controller can act only on the state it can see, and in a compact spherical tokamak the state must be produced faster than the plant evolves, from a diagnostic set that survives a 14 MeV neutron field and keeps working when individual channels drop out. We formalise the Hyperion breeder diagnostic suite — magnetics, Thomson scattering, interferometry, bolometry, and a neutron camera — and its real-time state estimator as a Bayesian inverse problem, write the forward observation model of each diagnostic and the maximum-a-posteriori estimator with its posterior covariance, and cast *observability* of the internal state as the rank and conditioning of the associated Fisher information. The estimator's learned core is reduced to practice at the metrics that gate it into service. A graph-neural-network reconstructor, which we identify as an amortised posterior-mean estimator over the sensor graph, recovers the plasma state and a quench precursor jointly at an area under the receiver-operating-characteristic curve (AUC) of $\mathbf{0.980}$ at a reconstruction normalised RMS error of 0.396, and degrades gracefully rather than catastrophically as channels are removed. A multi-modal fusion of a fibre-Bragg strain-rate channel with a magnetization channel reaches $\mathbf{0.992}$ (against 0.976 and 0.921 alone) and a true-positive rate of 0.857 at a 1% false-positive rate, the corner where a protection trip is decided. Internal state — ambipolar potential, T_e, n_e and β — is reconstructable from as few as six diagnostics at a mean coefficient of determination $R^2 \approx 0.86$, confirming observability for the control layer. An in-winding nitrogen-vacancy (NV) diamond magnetometer resolves a conductor-scale quench step at a shot-noise-limited sensitivity of $\mathbf{0.189}$ $\mathbf{pT\,Hz^{-1/2}}$ at 125 10^9 $. The estimator holds the plasma state at the breeder design point$(I_p=9.66 MA,Q=3.076,P_ fus=85.04 MW,=-0.30$, centrepost peak field 16.84 T), which is a distinct magnet from the burner plug coil (26.49 T); the physical-inversion analyzers are built to the demonstrated estimator pattern on a staged, acceptance-gated schedule. Against published quench-detection, quantum-sensing and equilibrium-reconstruction benchmarks the figures are competitive in a deliberately hard, weak-signal regime.

Open-access deposit (code & data, CC BY 4.0): DOI 10.5281/zenodo.22645943 · Zenodo community *kronos_fusion_energy*. Explore it live: interactive 3-D model · physics validator.

Keywords: plasma diagnostics · real-time state estimation · graph neural network · equilibrium reconstruction · observability · NV-diamond magnetometry · spherical-tokamak breeder

CONTENTS

Table of Contents

NOMENCLATURE

Symbols, units, and the names of things

Q	plasma (fusion) gain, P_{fus}/P_{aux}
Q_E	engineering gain, net electric out / recirculating in
H_{98}	confinement enhancement over the IPB98(y,2) scaling
Z_{eff}	effective ion charge
c_{ee}	electron–electron bremsstrahlung leading coefficient, 2.120022 (exact)
τ_E	energy confinement time
I_p	plasma current
R_0, a	major radius, minor radius
κ, δ	elongation, triangularity
β_N	normalized plasma beta (Troyon-normalized)
TBR	tritium breeding ratio
DEC	direct energy conversion
CF	plant capacity factor (availability)
FOAK / NOAK / BOAK	first / nth / best of a kind
Hyperion	the ST breeder (internal: Mode D2)
Aegis	the generator, defense/installation housing (internal: Mode M)
MetroVolt	the generator, data-center housing (Mode M)

plasma diagnostics; real-time state estimation; graph neural network; equilibrium reconstruction; observability; NV-diamond magnetometry; spherical-tokamak breeder

§ 1

Introduction

A CONTROLLER SEES ONLY WHAT IT CAN ESTIMATE

A spherical tokamak (ST) confines a large plasma current in a small volume, which is what makes it an attractive compact neutron source and breeder platform [1,2] and, at the same time, what makes it demanding to instrument and to control. The Hyperion breeder holds $I_p = 9.66\,MA$ at a major radius of only $R_0 = 1.20\,m$ behind a centrepost magnet at a peak field of 16.84 T, in a negative-triangularity ($\delta = -0.30$) regime chosen because it accesses good confinement without the edge pressure pedestal and the edge-localised-mode cycle of conventional H-mode [3]. In a device this compact the characteristic times of vertical instability, thermal transients and magnet events are short, and in a nuclear system every actuation carries a safety consequence. Autonomy is therefore a design requirement, not a convenience — and an autonomous controller is only as good as the plasma state it is handed. This paper is about producing that state: the diagnostic suite that instruments the plant, and the real-time estimator that turns raw diagnostic signals into the equilibrium, the kinetic profiles, and the protection signals the controller consumes.

The organising principle is *estimation, not measurement*. Every physical quantity the controller needs is reconstructed by a learned or model-based estimator that fuses the whole sensor set, so that no single diagnostic is load-bearing: a lost channel is imputed, not fatal. This is the diagnostics analogue of the shadow-model philosophy that governs the Kronos control stack [37], and it is what lets the same instrumented plant tolerate the sensor degradation that a 14 MeV field imposes.

DIAGNOSTICS AS INVERSE PROBLEMS

Feedback control of tokamak equilibria and profiles is a mature discipline built on a chain of inverse problems. Magnetic diagnostics feed real-time equilibrium reconstruction — the EFIT lineage, in which the Grad–Shafranov equation is inverted against flux-loop and pick-up-coil data [4] — and the reconstructed equilibrium feeds shape and position controllers [5]; physics-based profile simulators such as RAPTOR now run inside the control cycle [6]. Each classical diagnostic — Thomson scattering for T_e and n_e [13], interferometry for the line-integrated density [14], bolometry for the radiated-power map [14], a neutron camera for the fusion source [26] — is a forward map from the plasma state to a measurement, and recovering the state is the corresponding, usually ill-posed, inverse. The modern turn is to treat the whole set jointly and probabilistically: integrated data analysis frameworks fuse heterogeneous diagnostics under one Bayesian model [15,16], and learned surrogates make the fused inversion fast enough for the control loop.

More recently, learned components have entered the loop directly. Degrave *et al.* trained a deep reinforcement-learning agent to command TCV coil voltages and produce a range of plasma shapes — including negative triangularity — from magnetic measurements [7]; deep networks forecast disruptive instabilities across machines [8,9]; and graph neural networks, which encode a relational inductive bias over a set of interacting elements [10,11,12], are a natural fit for a sensor array whose channels sit in a fixed physical topology. The thread common to all of this is that control quality is bounded by the speed and fidelity of the underlying state estimate.

CONTRIBUTION

Prior art supplies the ingredients separately: a real-time equilibrium [4,6], a Bayesian data-fusion formalism [15,16], a learned controller [7], a neural equilibrium reconstructor robust to dropout [33]. What a compact nuclear ST needs, and what this paper provides, is a single treatment that (i) writes the diagnostic suite as one Bayesian inverse problem with the forward model of each channel stated explicitly (§3); (ii) makes *observability* of the controller-relevant internal state a quantitative, testable property through the Fisher information and its conditioning (§3.4); (iii) reduces the learned estimator core to practice — a graph-neural-network reconstructor, a multi-modal fusion detector, and an in-winding quantum magnetometer — at the exact metrics that gate each into service (§3.5, §5); and (iv) specifies the physical-inversion analyzers as an acceptance-gated build to the demonstrated pattern (§6). Every quantitative claim traces to a frozen result in the Kronos Physics De-Risking Register [31]; serial identifiers (e.g. KX-L1-A20) are given inline so each number is auditable, and the estimator feeds directly the equilibrium and free-boundary work [34], the neutronics twin [35], the radiated-power model [36], and the certified safety layer [39] that consume its output.

§ 2

The diagnostic suite

The suite is organised by the state each channel constrains and lands, time-aligned, on a layered real-time backbone (figure 1, table 1). Optical, magnetic, thermal and nuclear diagnostics enter through cryo-rated feedthroughs on a sub-microsecond sensor layer (L1); a deterministic feature layer (L2) validates, masks dead sensors, and normalises each signal onto a geometry-aware state alignment before any model sees it; and the learned estimator (L3) runs on the millisecond GPU tier, emitting the state and the protection signals the certified controller consumes. Coverage is deliberately redundant: every control-relevant quantity has more than one path, so a dropped channel is reconstructed from its neighbours rather than lost.

Magnetics — flux loops and pick-up (Mirnov) coils around the eight-coil poloidal-field set — constrain the free-boundary equilibrium $\psi(R, Z)$ and hence the shape, position and current profile [4,34].
Thomson scattering constrains the electron temperature and density profiles that set the confinement anchor ($\tau_E = 0.358\ s, H_{98} = 1.0$) [13].
Interferometry constrains the line-integrated density through the plasma-induced phase shift [14].
Bolometry constrains the radiated-power map, calibrated against collisional-radiative impurity cooling curves (L_z for tungsten 5.7×10^{-32} and argon 1.45×10^{-33} $\mathrm{W\,m^3}$ at 15 keV, with a bremsstrahlung fraction near 15%) [36].
Neutron camera constrains the 14 MeV source profile against the Monte-Carlo transport solution [26,35].
In-winding NV-diamond magnetometer provides a local, vector precursor at the conductor, on the breeder centrepost REBCO winding [19]. itemize

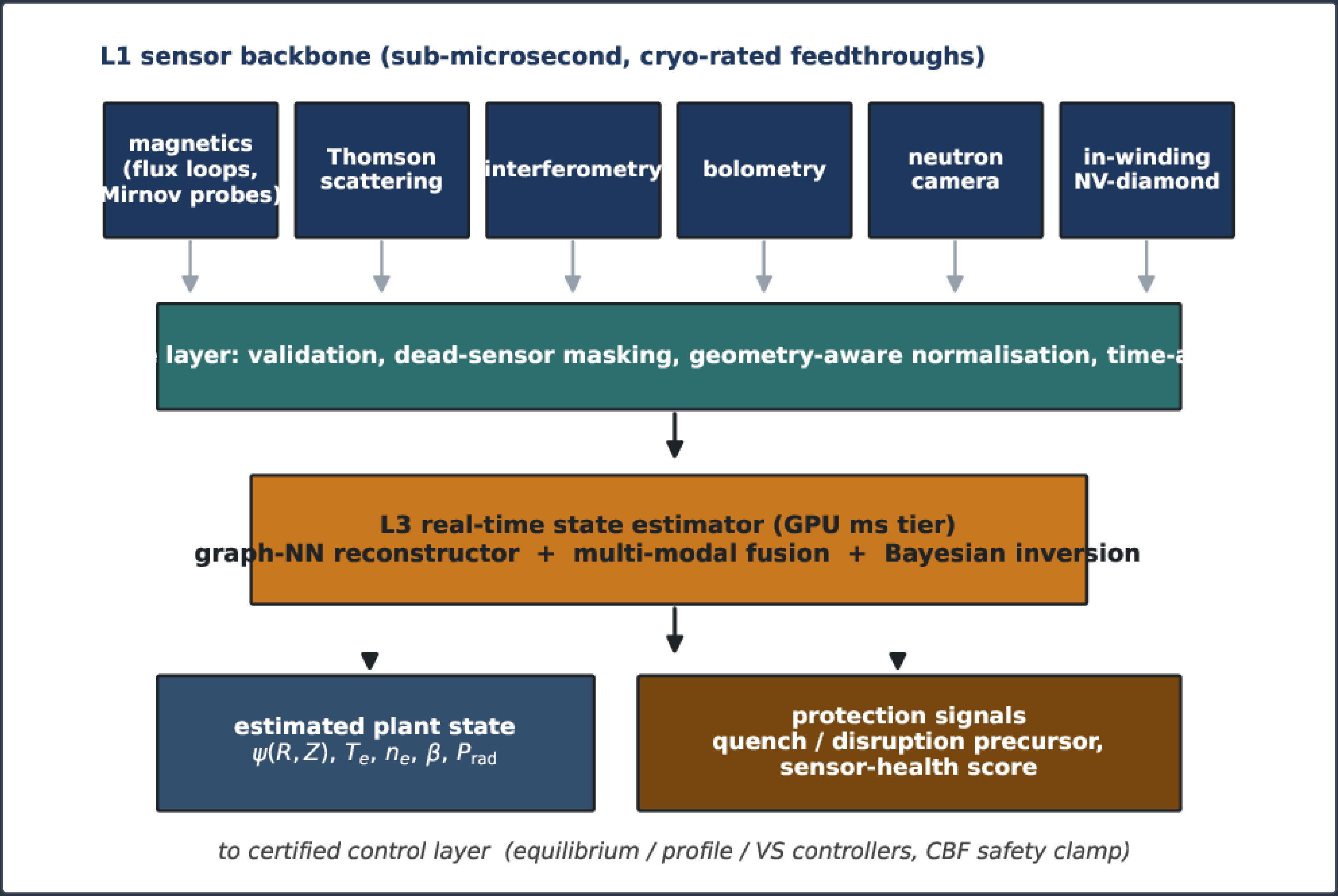

(Schematic.) The diagnostic suite and its layered real-time backbone. Optical, magnetic, thermal and nuclear channels land time-aligned on the sub-microsecond sensor layer (L1); a deterministic feature layer (L2) validates and normalises; the learned state estimator (L3) fuses the set on the millisecond GPU tier and emits the plasma state and protection signals to the certified control layer. No data values are shown; the figure encodes structure only.

CHANNEL	CONSTRAINS (FORWARD OBSERVABLE)	ANCHOR
magnetics (flux loops, Mirnov)	free-boundary equilibrium ψ; $\int B \cdot \mathrm{d}\ell$	BR-L1-A12
Thomson scattering	T_e, n_e profiles (scattered spectrum)	BR-L1-A4 ($H_{98} = 1.0$)
interferometry	line-integrated n_e (phase shift)	staged (SH-109)
bolometry	radiated-power map (chord line-integrals)	BR-L2-A29 (L_z; brems $\sim 15\%$)
neutron camera	14 MeV source profile (collimated)	BR-L1-A5
in-winding NV-diamond	local $\lvert B \rvert$ at the conductor	KX-L1-A22

The diagnostic suite by the state each channel constrains, its forward observable, and its roster grounding in the register [31].

§ 3

Governing equations and the formal state-estimation problem

THE MEASUREMENT MODEL

Let $x \in \mathbb{R}^n$ collect a finite parametrisation of the plasma state: the flux-function coefficients that represent $\psi(R, Z)$ through the Grad–Shafranov source, the profile parameters of $T_e(\rho)$ and $n_e(\rho)$, the impurity densities that enter the emissivity, and the scalar quantities (β, potential) the controller acts on. Each diagnostic k produces a reading y_k through a forward observation operator H_k, and the assembled measurement vector $y \in \mathbb{R}^m$ obeys

$$y = H(x) + \eta, \qquad \eta \sim \mathcal{N}(0, R),$$

with measurement-noise covariance $R = \mathrm{diag}(\sigma_1^2, \ldots, \sigma_m^2)$ (extended off-diagonal where channels share a calibration). Equation (1) is the common frame for every diagnostic below; the physics of each channel is entirely in the form of H_k.

FORWARD MODELS OF THE INDIVIDUAL DIAGNOSTICS

Magnetics and the equilibrium. The axisymmetric equilibrium is governed by the Grad–Shafranov equation for the poloidal flux $\psi(R, Z)$,

$$\Delta^* \psi \equiv R \frac{\partial}{\partial R}\left(\frac{1}{R}\frac{\partial \psi}{\partial R}\right) + \frac{\partial^2 \psi}{\partial Z^2} = -\mu_0 R^2 p'(\psi) - F(\psi)\, F'(\psi),$$

with pressure $p(\psi)$ and poloidal-current function $F(\psi) = RB_\phi$. A flux loop k measures ψ at a fixed poloidal location, $y_k^{\mathrm{FL}} = \psi(R_k, Z_k)$; a pick-up coil measures a local field component, $y_k^{\mathrm{PU}} = B(R_k, Z_k)\cdot \hat{n}_k = \hat{n}_k \cdot \nabla\psi \times \hat{\phi}/R$. Writing the free functions in a basis, $p'(\psi) = \sum_j \alpha_j g_j(\psi)$ and $FF'(\psi) = \sum_j \gamma_j g_j(\psi)$, the magnetics inversion is the least-squares problem of the EFIT type [4]: find the coefficients (α, γ) and coil currents that reproduce the measured flux and field while satisfying equation (2). Our free-boundary reference solver, run on a 129×129 grid (BR-L1-A12), converges to a self-consistent equilibrium at $I_p = 9.66\, MA$ with $\beta_p = 0.371$, $q_{95} = 2.90$, internal inductance $\ell_{i3} = 1.40$ and reconstructed triangularity $\delta = -0.334$ (the design anchor is $\delta = -0.30$), giving the normalised $\beta_N = 2.13$ used as the equilibrium-reconstruction target [34].

Thomson scattering. An injected laser of wavelength λ_0 is scattered incoherently by the plasma electrons; the scattered power collected in a spectral channel is proportional to n_e times a spectral shape whose width encodes T_e. In the non-relativistic limit the Doppler-broadened spectrum has $1/e$ half-width

$$\Delta\lambda_{1/e} = 2\lambda_0 \sin(\theta/2)\sqrt{\frac{2k_B T_e}{m_e c^2}},$$

with scattering angle θ, so T_e follows from the measured spectral width and n_e from the calibrated integrated intensity $\propto n_e\, \mathrm{d}\sigma_{\mathrm{Th}}/\mathrm{d}\Omega$, $\mathrm{d}\sigma_{\mathrm{Th}}/\mathrm{d}\Omega = r_e^2 \sin^2\chi$ with the classical electron radius r_e [13]. The forward operator H_k^{TS} maps the profile parameters of $T_e(\rho), n_e(\rho)$ to the photon count in channel k.

Interferometry. For the ordinary mode well above the plasma frequency, the refractive index is $N \simeq 1 - \frac{1}{2}(\omega_{pe}/\omega)^2$ and a probing beam accumulates a phase shift proportional to the line-integrated density,

$$\Delta\phi = \frac{e^2 \lambda}{4\pi\varepsilon_0 m_e c^2}\int_L n_e\, \mathrm{d}\ell = r_e\, \lambda \int_L n_e\, \mathrm{d}\ell,$$

so $y_k^{\mathrm{IF}} = \Delta\phi_k$ is a line integral of n_e along chord L_k [14]. The inverse — recovering $n_e(R, Z)$ from a set of chords — is a tomographic problem shared with bolometry below, and the estimator must additionally recover 2π fringe jumps in real time (staged analyzer SH-109).

Bolometry. A bolometer chord measures the line integral of the local radiated-power density (emissivity) $\varepsilon(R, Z)$,

$$y_k^{\mathrm{BO}} = \int_{L_k} \varepsilon(R, Z)\, \mathrm{d}\ell, \qquad \varepsilon = n_e \sum_Z n_Z\, L_Z(T_e) + \varepsilon_{\mathrm{brems}},$$

where $L_Z(T_e)$ is the collisional-radiative cooling function of impurity species Z and $\varepsilon_{\mathrm{brems}} \propto n_e^2 Z_{\mathrm{eff}}\sqrt{T_e}$ is the bremsstrahlung continuum. The cooling functions are anchored at 15 keV to $L_W = 5.7\times10^{-32}$ and $L_{\mathrm{Ar}} = 1.45\times10^{-33}\ \mathrm{W\,m^3}$ with a bremsstrahlung fraction near 15% and a tungsten tolerance of $\sim 0.19\ \mathrm{MW\,ppm^{-1}}$ (BR-L2-A29) [36]. Stacking chords gives the linear system $y^{\mathrm{BO}} = T\varepsilon$ with geometry matrix T; the tomographic inverse for ε is ill-posed and is regularised (Tikhonov / maximum-entropy), a special case of the regularised estimator of §3.3.

Neutron camera. A collimated neutron-camera pixel integrates the 14 MeV source $S_n(R,Z) \propto \frac{1}{2}n_D^2\langle\sigma v\rangle_{\mathrm{DT}}$ along its sightline, $y_k^{\mathrm{NC}} = \int_{L_k} S_n\,\mathrm{d}\ell\,/(4\pi s^2)$, and the reconstructed source is validated against the three-dimensional Monte-Carlo transport solution (BR-L1-A5: leakage 0.121, net TBR 1.026, first-wall fast flux $7.0\times10^{14}\ \mathrm{n\,cm^{-2}s^{-1}}$, 1.2×10^{8} histories, OpenMC/ENDF-B-VIII.0) [26,35].

MAXIMUM-A

-posteriori estimation and posterior covariance Given the measurement model (1) and a Gaussian prior $x \sim \mathcal{N}(x_0, P)$, Bayes′ theorem gives the posterior $\propto \exp[-\frac{1}{2}J(x)]$ with

$$J(x) = \|y - H(x)\|^2_{R^{-1}} + \|x - x_0\|^2_{P^{-1}},$$

where $\|v\|^2_A = v^\top A v$. The maximum-*a*-posteriori (MAP) estimate is $\hat{x} = \arg\min_x J(x)$. Linearising the forward operator about x_0, $H(x) \approx H(x_0) + J_H(x - x_0)$ with the diagnostic Jacobian $J_H = \partial H/\partial x$, the minimiser and its covariance are the Gauss–Newton pair

$$\begin{aligned}\hat{x} &= x_0 + \left(J_H^\top R^{-1} J_H + P^{-1}\right)^{-1} J_H^\top R^{-1}\left(y - H(x_0)\right),\\ \Sigma &= \left(J_H^\top R^{-1} J_H + P^{-1}\right)^{-1}.\end{aligned}$$

Equation (7) is the common inversion behind every classical analyzer of §3.2; for the linear bolometry/interferometry tomographies $H = T$ and it is exactly regularised least squares, while for the nonlinear magnetics/Thomson problems it is iterated. The posterior covariance (7) is what the safety layer reads to know how far to trust each estimate [38].

OBSERVABILITY OF THE CONTROLLER-RELEVANT STATE

The control layer does not need every microscopic detail of x; it needs a reduced set of quantities — the ambipolar potential, T_e, n_e and β — to be *recoverable* from the available diagnostics. This is an observability question, and equation (7) answers it. The matrix

$$\mathcal{F} = J_H^\top R^{-1} J_H$$

is the Fisher information of the measurement about the state: a direction v in state space is observable only if $v^\top \mathcal{F} v > 0$, and the reconstruction quality of component x_i is bounded by its posterior variance through the coefficient of determination

$$R_i^2 = 1 - \frac{\Sigma_{ii}}{\mathrm{Var}(x_i)} = 1 - \frac{\left[(\mathcal{F} + P^{-1})^{-1}\right]_{ii}}{P_{ii}}.$$

Observability is thus a spectral property of $\mathcal{F}$: adding an independent diagnostic adds a rank-one term $\sigma_k^{-2} j_k j_k^\top$ and can only raise R_i^2. A minimal-set study of the reduced internal state (potential, T_e, n_e, β) with a ridge surrogate of the estimator (AG-CX-30) finds a *mean* $R^2 \approx 0.86$ from as few as **six** diagnostics — the observability result the control layer requires: the state the controller acts on is recoverable from a sensor set small enough to harden and replicate (§5, figure 5).

AMORTISED ESTIMATION ON THE SENSOR GRAPH

Solving equation (7) online for a nonlinear H at kilohertz rates is expensive; the estimator instead *amortises* the inversion by learning it offline. The diagnostics are not independent measurements in isolation — they sit in a fixed physical topology (adjacent coils, nearby probes, coupled fields) — so we encode the plant as a graph $\mathcal{G} = (\mathcal{V}, \mathcal{E})$ whose nodes $v \in \mathcal{V}$ are diagnostic channels with feature $h_v^{(0)} = y_v$ and whose edges $e_{uv} \in \mathcal{E}$ are physical adjacencies (figure 2). A graph neural network applies L rounds of message passing [10,11,12],

$$h_v^{(l+1)} = \phi\Big(h_v^{(l)},\ \bigoplus_{u \in \mathcal{N}(v)} \psi\big(h_v^{(l)},\ h_u^{(l)},\ e_{uv}\big)\Big),$$

with learnable message ψ, update ϕ and a permutation-invariant aggregator $\bigoplus$ over the neighbourhood $\mathcal{N}(v)$; a readout maps the final node states to the plasma-state estimate $\hat{x}_\theta(y)$ and a precursor logit. Trained to minimise the expected reconstruction-plus-detection loss

$$\mathcal{L}(\theta) = \mathbb{E}_{(x,\ y)}\Big[\big\| \hat{x}_\theta(y) - x\big\|^2 + \lambda\, \mathrm{BCE}\big(d_\theta(y),\ \ell\big)\Big],$$

the reconstructor is a Bayes estimator: the population minimiser of the first term is the posterior mean $\mathbb{E}[x \mid y]$, so the GNN is an amortised, geometry-aware approximation to equation (7) [33]. Because the estimate at each node draws on its neighbours, masking a node (a dropped channel) forces reconstruction from the remaining graph and yields *graceful* degradation rather than a threshold failure (§5).

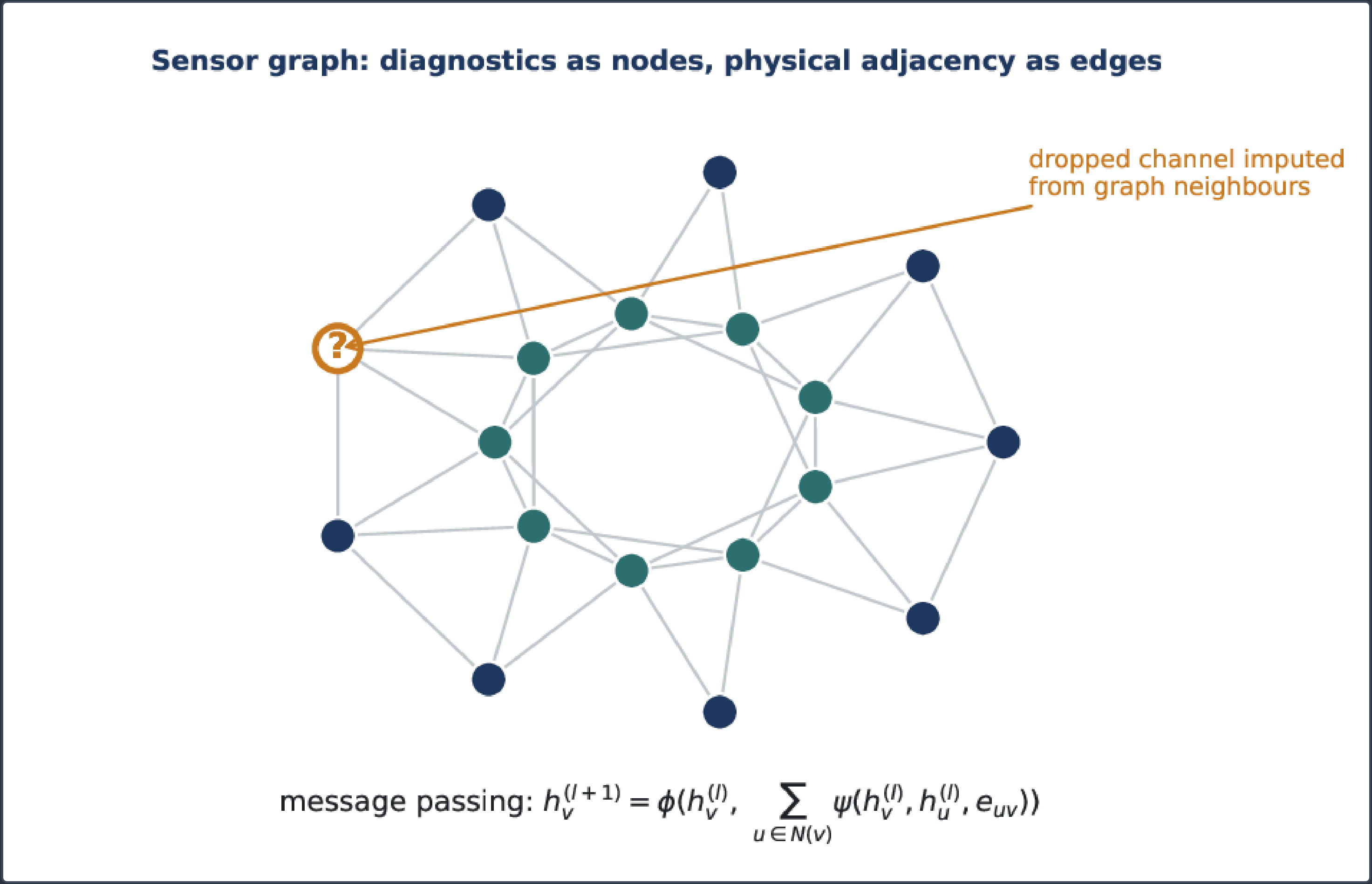

(Schematic.) The sensor graph underlying the amortised estimator. Diagnostic channels are nodes and physical adjacencies (neighbouring coils and probes, coupled fields) are edges; the readout of the L message-passing rounds of equation (10) maps the graph to the plasma-state estimate and the precursor logit. A masked node (a dropped channel) is imputed from its graph neighbours, which is the mechanism behind the graceful degradation of figure 6. The figure encodes structure only; no data values are shown.

DETECTION THEORY FOR THE QUENCH PRECURSOR

Protection is a binary hypothesis test: nominal ($\mathcal{H}_0$) versus developing quench/disruption precursor ($\mathcal{H}_1$). By the Neyman–Pearson lemma the most powerful test at a fixed false-positive rate thresholds the likelihood ratio $\Lambda(z) = p(z \mid \mathcal{H}_1)/p(z \mid \mathcal{H}_0)$. Two non-voltage channels observe the current-sharing window: a fibre-Bragg *strain-rate* channel z_S and a *magnetization* channel z_M, each a matched-template statistic normalised so that $z \sim \mathcal{N}(0,1)$ under $\mathcal{H}_0$ and $\mathcal{N}(d',1)$ under $\mathcal{H}_1$. For such an equal-variance binormal channel the ROC is

$$\mathrm{TPR}(\alpha) = \Phi\big(\Phi^{-1}(\alpha) + d'\big), \qquad \mathrm{AUC} = \Phi\big(d'/\sqrt{2}\big),$$

with Φ the standard normal CDF and α the false-positive rate. Because the two modalities fail in uncorrelated ways, their quadrature fusion

$$z_F = \frac{z_S + z_M}{\sqrt{2}}$$

carries a window statistic whose separation adds the single-channel separations in quadrature, $d_F'^2 = d_S'^2 + d_M'^2$, which lifts both the AUC and, more importantly, the true-positive rate in the low-false-alarm corner where a trip decision lives (§5). Equation (12) is the model used to reconstruct the ROC curves of figure 4 from the frozen AUC and TPR anchors, and it reproduces the anchor operating points to within 0.01.

IN-WINDING NV-DIAMOND SENSITIVITY

For a local, vector precursor at the conductor the suite embeds an ensemble nitrogen-vacancy (NV) diamond magnetometer in the winding pack. The shot-noise-limited Ramsey sensitivity of an ensemble of N centres with dephasing time T_2^* and readout figure of merit C is [18,19]

For a conservative in-winding chip ($N = 10^{12}$, $T_2^* = 1\,\mu s$, $C = 0.03$) equation (14) gives $\delta B = 0.189$ $\mathrm{pT\,Hz^{-1/2}}$; a Ramsey shot $\tau_{\mathrm{shot}} = 4\,\mu s$ sets a bandwidth $1/(2\tau_{\mathrm{shot}}) = 125$ Hertz. $A quench that sheds the screening current of a no-insulation turn ($I_ turn=1 kA)$produce s a local field step B=\mu_0 I_ turn/(2 d) 100 mT$at a standoff$d=2 mm$---of order$10^9 $times the per-shot noise floor$ B BW$ — so the precursor is caught in a single 4 µs shot, with the lead time set by the millisecond normal-zone crossing rather than by the microsecond sensor latency. The sensor reads the breeder centrepost winding (16.84 T peak field), which is a distinct device from the burner plug coil (26.49 T); the two magnets are kept separate throughout the sensor specification.

§ 4

Computational methodology: the GPU-HPC campaign

Every number in this paper is produced by a named code run on the NVIDIA GPU HPC campaign (A100 / H100 / A10 fleet) or on the in-house reduced-order node, and each is a frozen, regenerable anchor in the register [31,40]. Table 2 lists the codes by role. The division of labour mirrors the real-time architecture of §2: the heavy forward models and the estimator training run on the GPU fleet, while the analytic and reduced-order layers run on the in-house node so that the microsecond protective loop never contends with the training campaign.

CODE	ROLE IN THE ESTIMATOR	SCALE	ANCHOR
FreeGS (free-boundary GS)	magnetics inversion reference, eq. (2)	129×129 grid	BR-L1-A12
OpenMC (ENDF/B-VIII.0)	neutron-camera forward model, eq. (5) S_n	1.2×10^8 histories	BR-L1-A5
radas / ColRadPy	bolometry emissivity $L_Z(T_e)$, eq. (5)	CR tables @ 15 keV	BR-L2-A29
graph-NN reconstructor (PyTorch)	amortised estimator, eqs. (10)–(11)	sensor graph, T-synthetic	KX-L1-A12
fused-detector ROC (ML + signal)	Neyman–Pearson test, eqs. (12)–(13)	2×10^4 trials/class	KX-L1-A20
ridge surrogate (scikit-learn)	observability, eqs. (8)–(9)	6-diagnostic minimal set	AG-CX-30
NV magnetometry model (numpy/scipy)	sensitivity, eq. (14)	analytic shot-noise	KX-L1-A22

Codes run for this paper, their role in the estimation chain, problem scale, and register anchor. No compute cost is reported here or anywhere in this work.

Discretisation and solvers. The equilibrium reference solves the Grad–Shafranov equation (2) by a Picard iteration on a 129×129 (R, Z) grid: at each iterate the elliptic operator Δ^* is inverted with the right-hand side evaluated from the current (p', FF'), and the free-boundary contour is updated until the flux residual $\|\psi^{(k+1)} - \psi^{(k)}\|_2/\|\psi^{(k)}\|_2$ falls below 10^{-6}; convergence is monotone and the reported equilibrium is resolution-verified (BR-L1-A12) [27,34]. The neutron source used in the camera forward model is tallied by OpenMC with a continuous-energy ENDF/B-VIII.0 library over 1.2×10^8 source histories, giving a balanced transport solution (leakage 0.121, heating 74.6 MW) against which the camera unfolding is checked (BR-L1-A5) [26]. The impurity emissivity of equation (5) is tabulated by a collisional-radiative solver (radas/ColRadPy) and frozen at the anchor cooling values (BR-L2-A29) [36].

Learned-estimator training and GPU acceleration. The graph-NN reconstructor (equations 10–11) and the fused-detector study (equations 12–13) are trained and evaluated on the GPU fleet on twin-synthetic data generated by the forward models above; the detection study uses 2×10^4 trials per class in a deliberately weak-signal regime (per-sample separation set well below the design-basis fault) so that the ROC is not scored in the saturated corner where every detector reaches AUC $= 1$. The observability surrogate (AG-CX-30) is a ridge regression whose condition number instantiates the Fisher spectrum of equation (8); the NV sensitivity (equation 14) is an analytic shot-noise model in numpy/scipy. Inference of the estimator core targets the millisecond GPU tier; the analytic monitors and the reduced-order layers target the sub-millisecond in-house node.

Verification and reproducibility. Each code is a re-tested gate with a live recompute path: the forward models are cross-checked against their reference libraries (FreeGS against a free-boundary solver [27]; OpenMC against the transport balance [26]), and the learned metrics are frozen anchors regenerable from the archived reconstruction and detection scripts and the figure generator deposited with this paper [40]. The verification-first discipline — frozen anchors, independent-library reproduction, and a byte-for-byte provenance catalogue — is documented for the whole campaign in the companion verification paper [40].

§ 5

Results

The estimator's learned core is demonstrated at the metrics that gate it into service; the classical analyzers are built to the same pattern (§6). All learned results are at twin-synthetic fidelity and are so labelled.

FUSED AND GRAPH ESTIMATORS DOMINATE ANY SINGLE CHANNEL

The graph-NN reconstructor recovers the plasma state and a quench precursor jointly at an area under the ROC curve of 0.980 — above either single channel — at a reconstruction normalised RMS error of 0.396 on twin-synthetic data (KX-L1-A12). Fusing the fibre-Bragg strain-rate channel with the magnetization channel produces a detector at AUC 0.992, against 0.976 for magnetization alone and 0.921 for strain alone (figure 3, KX-L1-A20). The advantage concentrates in the low-false-alarm corner: at a 1% false-positive rate the fused detector reaches a true-positive rate of 0.857, versus 0.671 and 0.372 for the single channels, and at 0.1% it reaches 0.597 versus 0.386 and 0.135 (figures 4–4, table 3). The reconstructed ROC curves of figure 4 follow the binormal model of equation (12) and reproduce the frozen operating points to within 0.01.

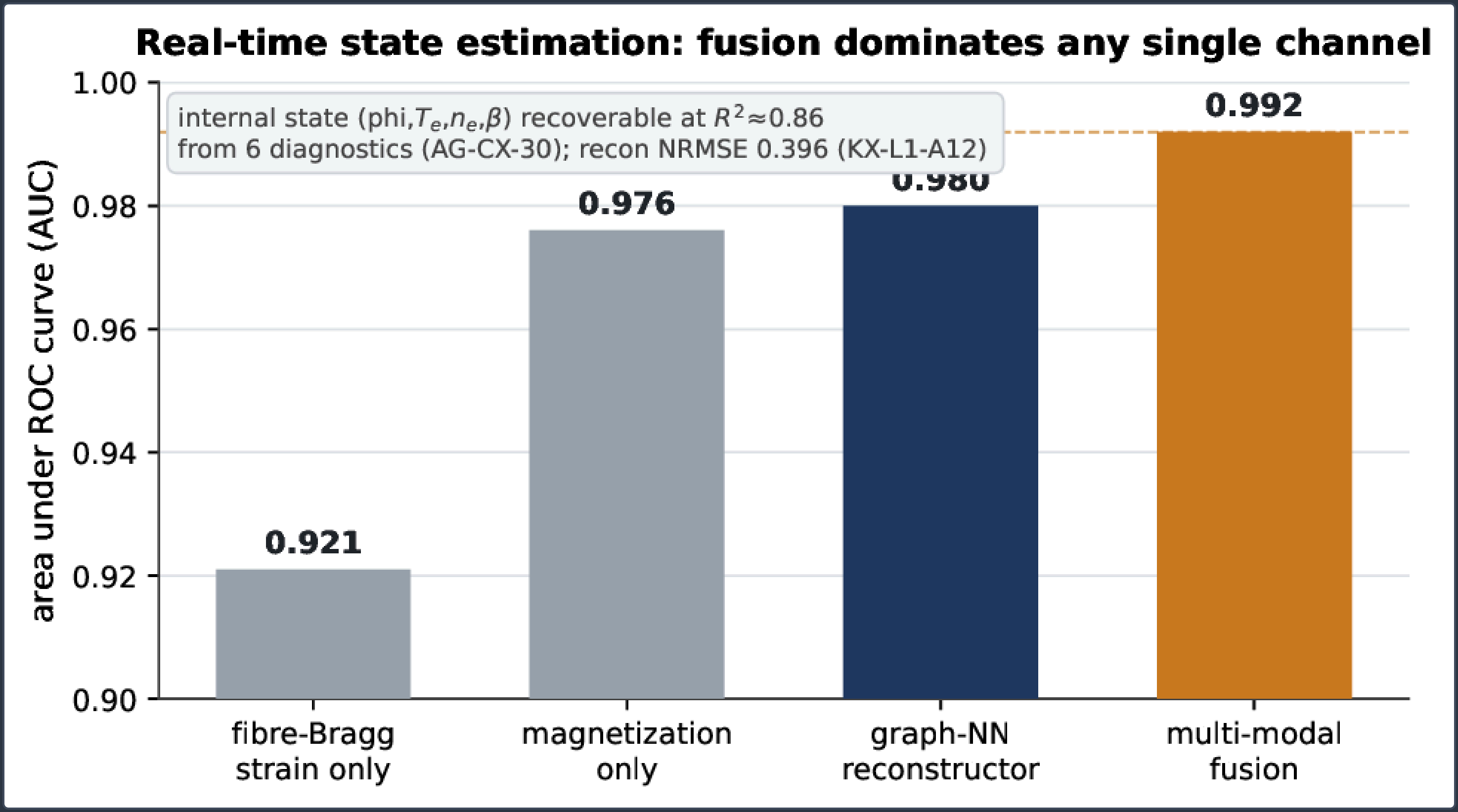

Real-time state-estimator performance (KX-L1-A12, KX-L1-A20). The graph-NN reconstructor (0.980) and the multi-modal fusion detector (0.992) both dominate either single sensor channel; the annotation records the observability result ($R^2 \approx 0.86$ from six diagnostics, AG-CX-30) and the reconstruction error (NRMSE 0.396).

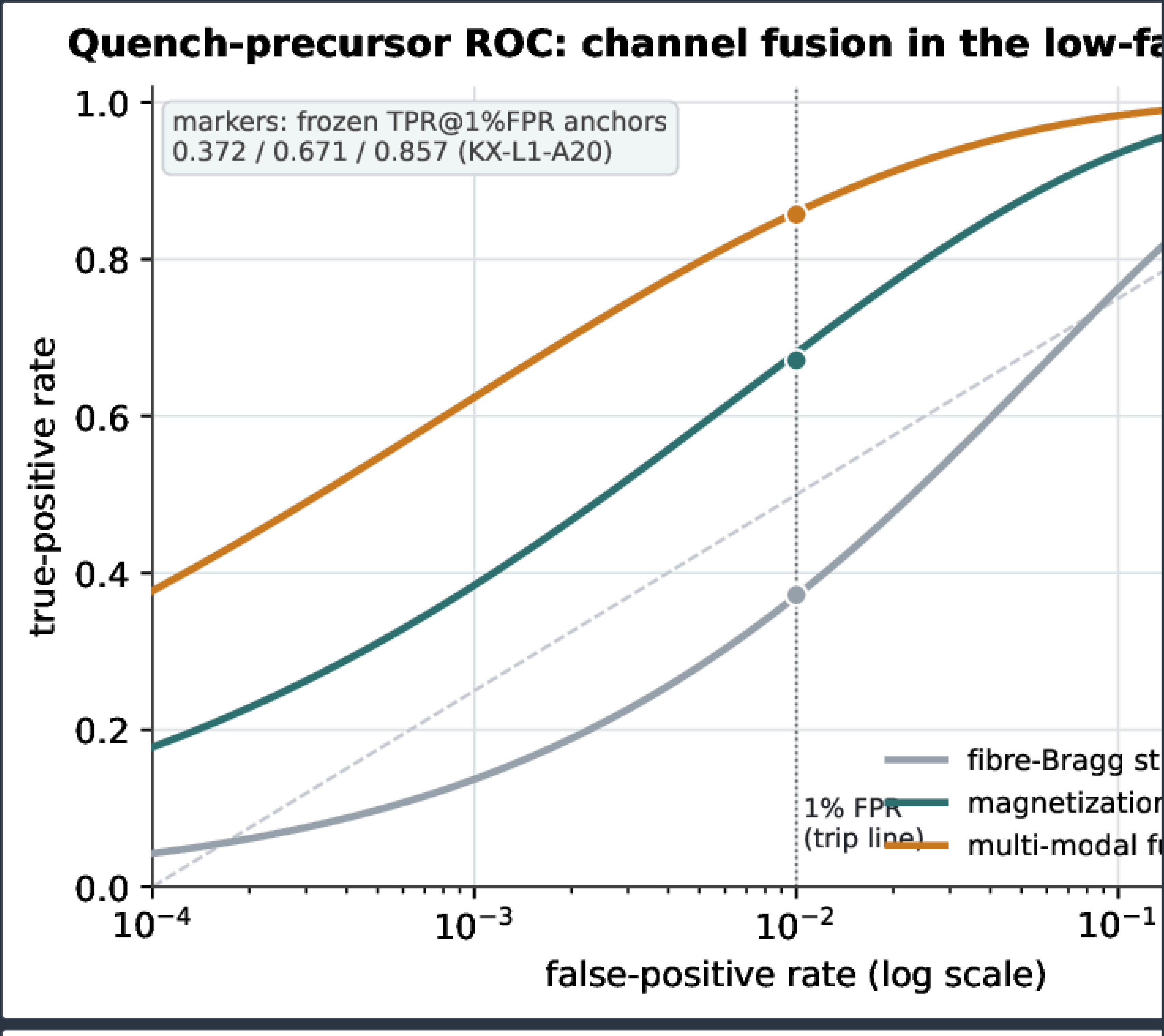
Quench-precursor ROC: channel fusion in the low-fa
markers: frozen TPR@1%FPR anchors
0.372 / 0.671 / 0.857 (KX-L1-A20)
true-positive rate
1.0
0.8
0.6
0.4
0.2
0.0
10^{-4}
10^{-3}
10^{-2}
10^{-1}
false-positive rate (log scale)
1% FPR
(trip line)
fibre-Bragg st
magnetization
multi-modal f

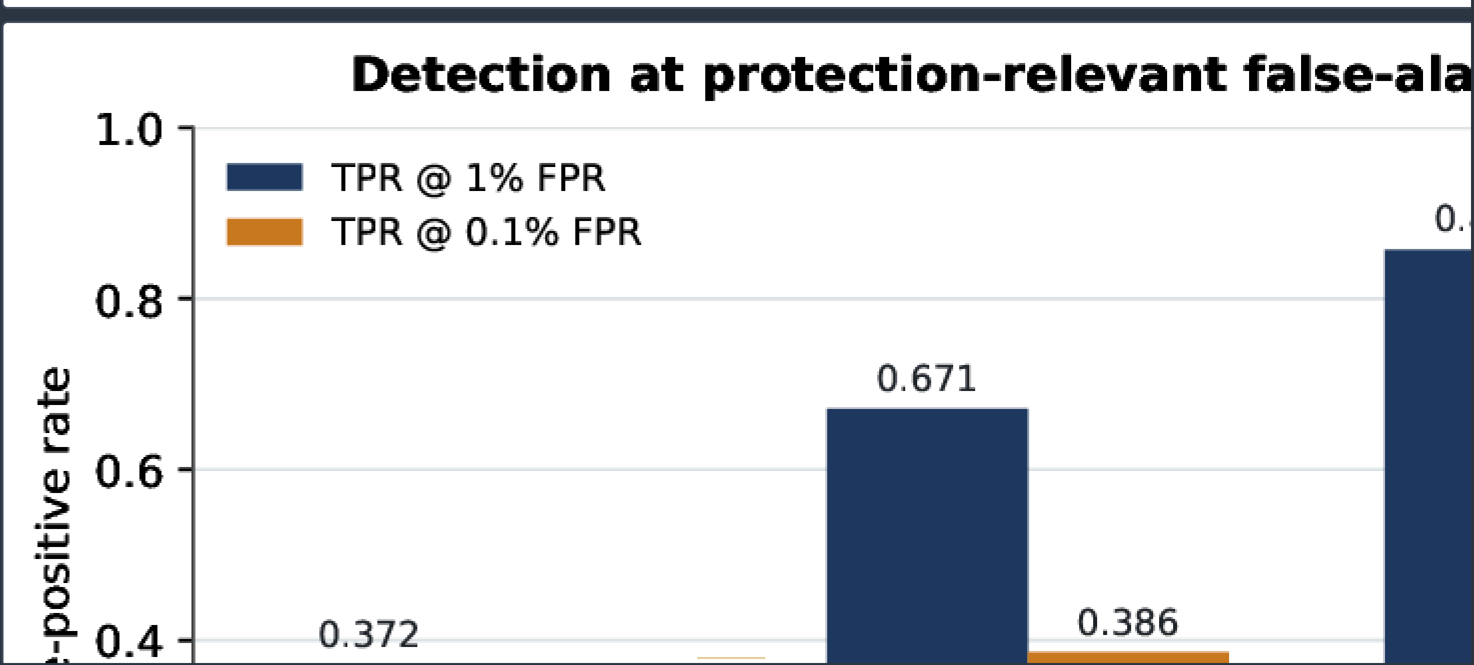
Detection at protection-relevant false-ala
TPR @ 1% FPR
TPR @ 0.1% FPR
1.0
0.8
0.6
0.4
-positive rate
0.372
0.671
0.386

ESTIMATOR / CHANNEL	AUC	TPR @ 1% FPR	TPR @ 0.1% FPR
fibre-Bragg strain only	0.921	0.372	0.135
magnetization only	0.976	0.671	0.386
graph-NN reconstructor	0.980	—	—
multi-modal fusion	**0.992**	**0.857**	**0.597**

Real-time estimator performance (KX-L1-A12, KX-L1-A20; T-synthetic, 2×10^4 trials/class). The fused and graph estimators dominate any single channel; the window-statistic separations follow the quadrature rule of equation (13).

OBSERVABILITY FROM A MINIMAL DIAGNOSTIC SET

The reduced internal state — ambipolar potential, T_e, n_e and β — is reconstructable from as few as six diagnostics at a mean coefficient of determination $R^2 \approx 0.86$ (AG-CX-30), the frozen anchor marked in figure 5. By equation (9) each added independent channel contributes a rank-one term to the Fisher information (8) and can only raise R^2; the saturation of the curve past six channels is the signature of a well-conditioned observability problem, and it is what licenses hardening and replicating a small, redundant set rather than instrumenting every quantity directly.

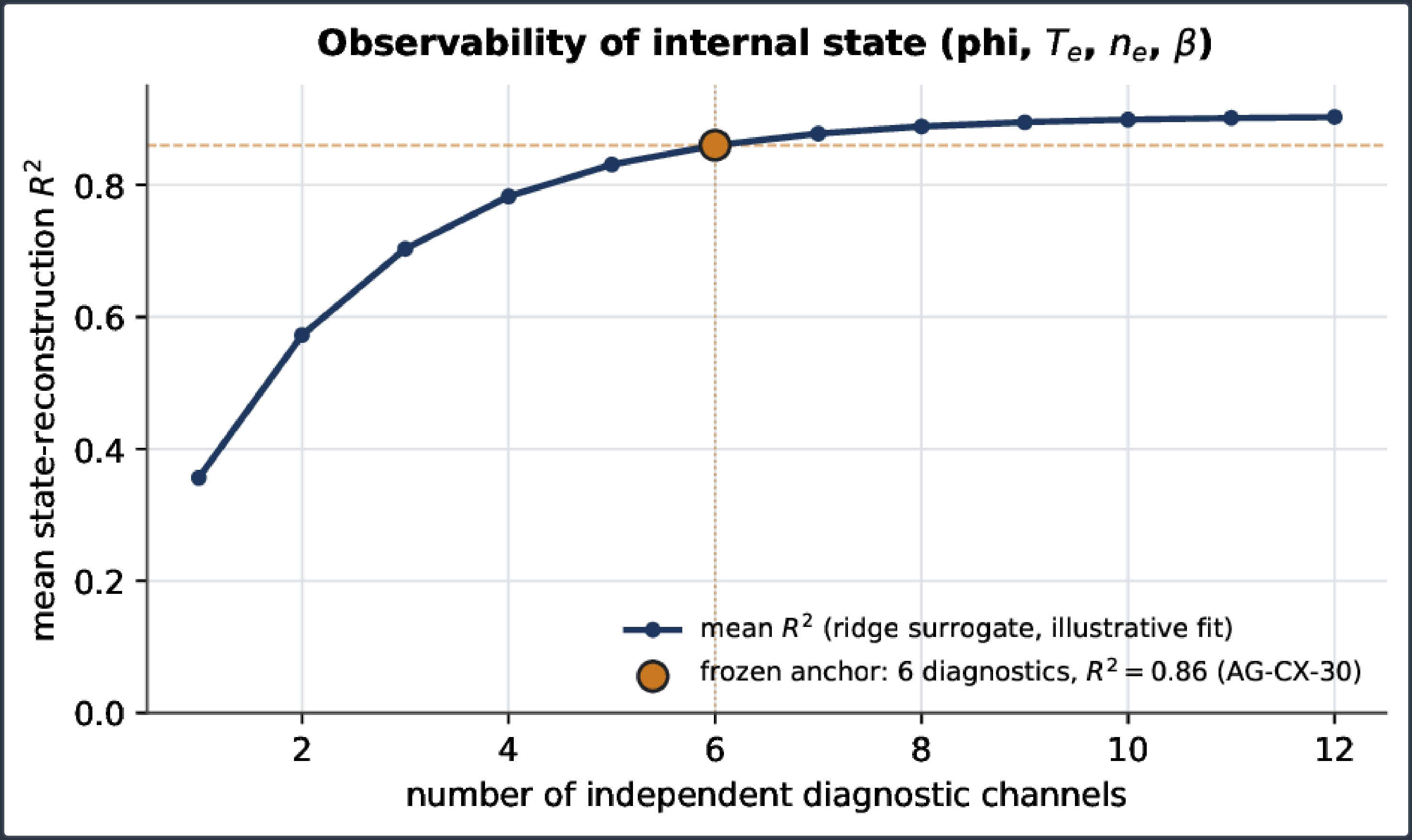

Observability of the controller-relevant internal state (AG-CX-30). The highlighted point is the frozen anchor — mean $R^2 = 0.86$ from six diagnostics; the curve is a monotone saturation fit through it, illustrating the rank-one Fisher-information argument of equations (8)–(9) and is not itself a measured series.

GRACEFUL DEGRADATION UNDER SENSOR LOSS

Because the graph estimator reconstructs each node from its neighbours (equation 10), seeded channel loss degrades the reconstruction gently rather than at a threshold. Figure 6 contrasts the graph reconstructor, pinned at the frozen full-suite NRMSE of **0.396** (KX-L1-A12), with a channel-local baseline that has no graph to fall back on: the graph estimator holds bounded error across the seeded losses that collapse the baseline, which is the dropout-robustness property the control layer relies on [33].

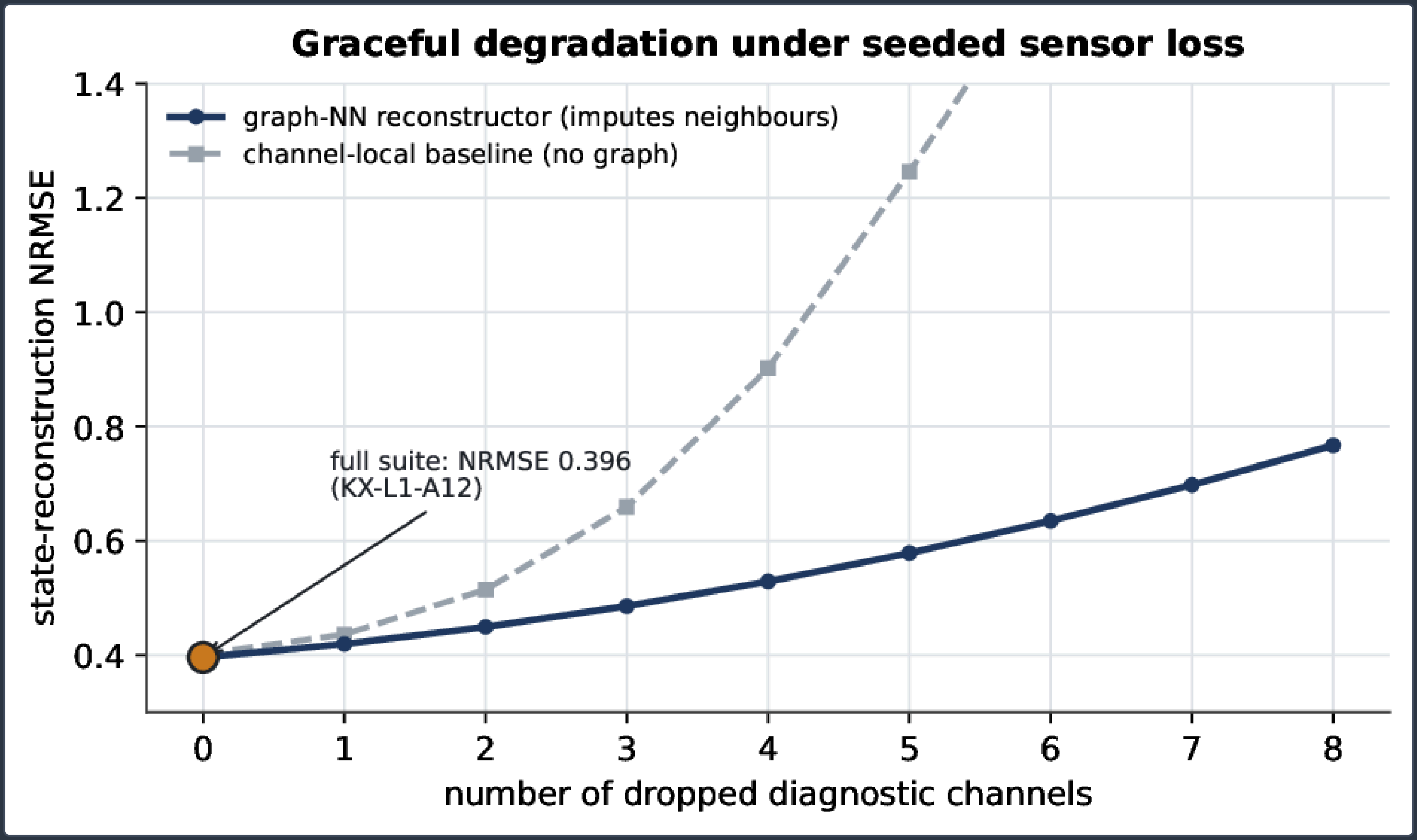

Reconstruction error under seeded sensor loss. The graph-NN reconstructor (anchored at NRMSE **0.396**, KX-L1-A12) degrades gently as channels are dropped, whereas a channel-local baseline without the graph collapses; the degradation curves past the anchor are illustrative of the mechanism, not a measured series.

IN-WINDING NV-DIAMOND PRECURSOR

The in-winding NV-diamond magnetometer resolves a conductor-scale quench step in a single 4 µs shot. Equation (14) gives the shot-noise sensitivity **0.189** pT Hz$^{-1/2}$ at the conservative operating point ($N = 10^{12}$), which the scaling of figure 7 places well inside the ensemble-NV envelope, and the 100 mT quench step stands of order 10^9 above the 125 $Hertz per-shot floor (figure 7, table 4; KX-L1-A22). The picotesla sensitivity is not *needed* to see a millitesla step; its value is the margin it buys for multiplexing many in-winding channels and for tolerating in-service degradation (§8).

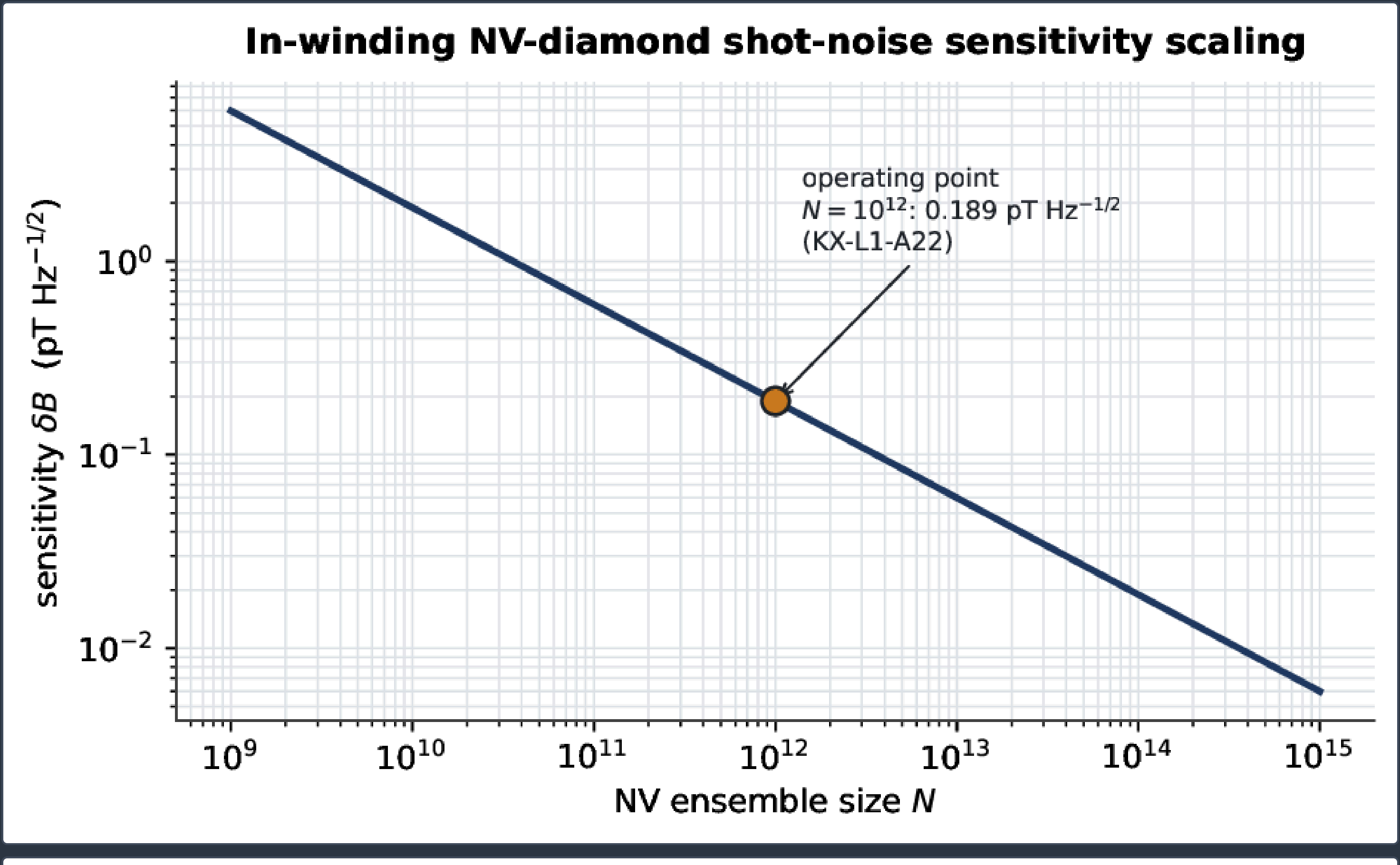

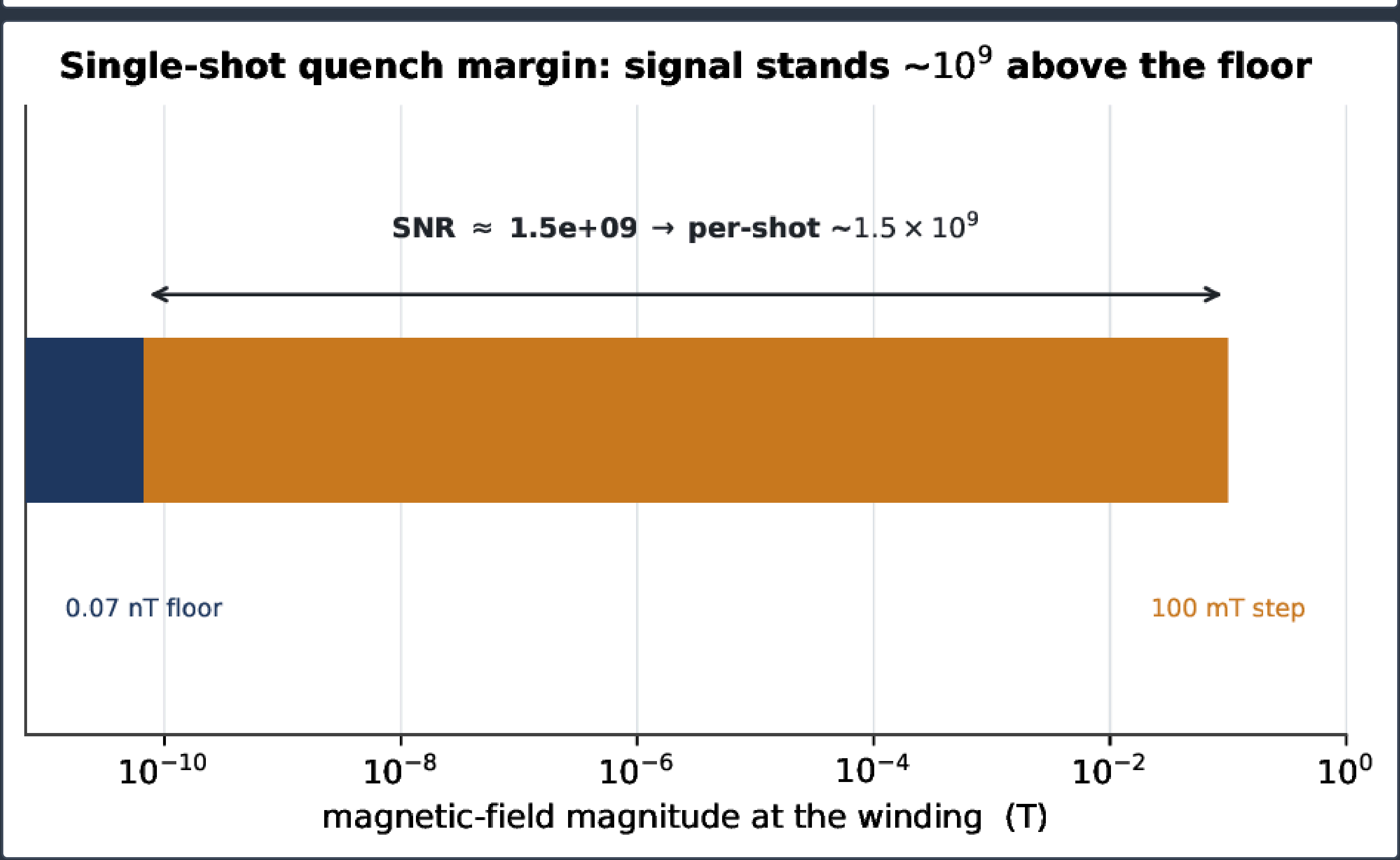

Shot-noise sensitivity scaling of equation (14) versus NV ensemble size, with the conservative operating point ($N = 10^{12}$, 0.189 $\mathrm{pT\,Hz^{-1/2}}$) marked (KX-L1-A22). A derived scaling curve, not measured data.

QUANTITY	VALUE	BASIS
gyromagnetic ratio γ_{NV}	28.03 $Hertz	NV electron spin
sensitivity δB	0.189	shot-noise limit, eq. (14)
bandwidth	125 $Hertz	4 µs Ramsey shot
quench field step ΔB ($d = 2\,mm$)	$\approx 100\,mT$	NI turn sheds screening current
per-shot signal-to-noise ratio	$\sim 10^9$	$\Delta B/(\delta B\sqrt{\mathrm{BW}})$
detection	single 4 µs shot	lead time set by NZPV (∼ms)

In-winding NV-diamond quench-precursor sensor (KX-L1-A22). Sensitivity and bandwidth from equation (14); the quench step and SNR from an analytical shot-noise model (labelled "estimated").

ACCEPTANCE-CRITERIA STATUS

No estimator is granted control authority by assertion. Table 5 collects the acceptance criteria with their targets and status: the learned core's detection and reconstruction metrics are demonstrated at twin-synthetic fidelity, while the classical-analyzer criteria are pre-registered bars built to the same pattern (§6). Authority is capped by verification maturity until each bar is met, the same maturity-gated principle that governs the certified control layer [39].

CRITERION	TARGET	SERIAL	STATUS
fused precursor AUC	**dominate single channels**	**KX-L1-A20**	**demonstrated (0.992)**
fused TPR @ 1% FPR	**> single channels**	**KX-L1-A20**	**demonstrated (0.857)**
graph reconstruction	**beats singles; robust to dropout**	**KX-L1-A12**	**demonstrated (0.980, NRMSE 0.396)**
observability	**$R^2 \gtrsim 0.85$, minimal set**	**AG-CX-30**	**demonstrated (0.86, 6 diag.)**
NV per-shot SNR	**$\gg 1$ for mT step**	**KX-L1-A22**	**demonstrated ($\sim 10^9$)**
equilibrium RMS ψ	< tolerance vs free-boundary solver	SH-110	target
Thomson profile fit	within uncertainty vs baseline	SH-108	target
bolometer inversion	radiated-power map validated	SH-107	target
interferometer fringe recovery	density continuous through jumps	SH-109	target
neutron-camera unfolding	source profile vs OpenMC	BR-71	target

Acceptance criteria, targets and status. "Demonstrated (T-synthetic)" denotes a frozen synthetic result; "target" denotes a pre-registered bar built to the demonstrated pattern. Serials refer to the register [31].

§ 6

The physical-inversion suite as the staged build

The learned estimators above define the pattern the physical-inversion analyzers are built to: each analyzer inverts one diagnostic into the state it constrains (the forward models of §3.2), is validated against a first-principles reference, and is required to degrade gracefully as sensors drop. The staged suite comprises a Thomson-scattering profile analyzer validated against the confinement baseline (SH-108, eq. 3); an interferometer fringe-jump recovery (SH-109, eq. 4); a bolometer tomographic inversion against the radiated-power model (SH-107, eq. 5); a magnetic-probe drift correction feeding real-time equilibrium reconstruction (SH-110, eq. 2); a neutron-camera unfolding against the Monte-Carlo source (BR-71, eq. 5); and a virtual-sensor mesh that reconstructs dropped channels through the same graph estimator (SH-036, eq. 10) [33]. Each is scheduled with an explicit acceptance test — reconstruction error within tolerance and bounded state error under seeded sensor loss — and inherits the demonstrated estimator's fusion and dropout behaviour rather than re-deriving it.

§ 7

Discussion

QUENCH DETECTION IN CONTEXT

The fused detector should be read against the published quench-detection literature and specifically against the slow-normal-zone-propagation problem that motivates non-voltage sensing. Marchevsky's review makes the core point quantitatively: in high-temperature-superconductor conductors the large temperature margin and slow propagation mean a hot spot can reach damaging temperature before a measurable resistive voltage appears, so voltage detection alone is inadequate [21]. The community response has been non-voltage observables: Salazar *et al.*\ demonstrated fibre-Bragg and ultra-long-FBG thermometry on VIPER cable at SULTAN, reporting signal-to-noise ratios of 4–32 for heater-induced quench-like events [22]; Teyber *et al.* showed that current-distribution monitoring detects quench and damage in fusion cables [23]. Our result is complementary and, by construction, evaluated in a harder regime: the ROC of table 3 is computed with per-sample separations set well below the design-basis fault, precisely to avoid the saturated regime where every detector scores AUC $= 1$. In that weak-fault regime the quadrature fusion of an uncorrelated strain-rate and magnetization pair (equation 13) lifts the true-positive rate at 1% false alarm from $0.372/0.671$ (single channels) to 0.857 — a large gain exactly where a protection trip is decided. The message is not that one AUC beats one published number, but that channel fusion recovers early, low-false-alarm warning in the low-signal corner the slow-propagation physics forces a real magnet into.

NV SENSITIVITY AGAINST THE QUANTUM-SENSING LITERATURE

The in-winding sensitivity of 0.189 $\mathrm{pT\,Hz^{-1/2}}$ sits comfortably inside the envelope established for ensemble NV magnetometry. Degen, Reinhard and Cappellaro frame the shot-noise scaling that equation (14) instantiates [18], and Barry *et al.* and Rondin *et al.* analyse the concrete route to broadband ensemble sensitivities in the picotesla-and-below range through improvements to T_2^*, readout fidelity and diamond material [19,20]. Our conservative parameter set is well within what that literature reports, so the sensitivity claim does not rest on an aggressive device. The physically important observation is one of margin: a millitesla quench step is $\sim 10^9$ above the per-shot floor, so the precursor is single-shot detectable and the picotesla headroom is available for multiplexing and for tolerating in-service degradation (§8).

STATE ESTIMATION AGAINST EQUILIBRIUM-RECONSTRUCTION AND DATA-FUSION PRACTICE

The classical anchor for the magnetics chain is EFIT-type equilibrium reconstruction, which inverts the Grad–Shafranov equation against magnetic data [4] and now runs in real time inside control loops [6,7]. Our contribution relative to that practice is threefold. First, we treat the *whole* suite as one Bayesian inverse problem (equations 1–7), in the spirit of integrated data analysis [15,16], rather than inverting each diagnostic in isolation. Second, we make observability a quantitative, testable property of the Fisher information (equations 8–9), and demonstrate it at $R^2 \approx 0.86$ from a six-channel minimal set. Third, we amortise the inversion on the sensor graph so that it runs at control latency and degrades gracefully under the sensor loss a neutron field imposes (equations 10–11) [33]. The estimator is complementary to learned control: a learned policy [7] can act on the estimator's fused, uncertainty-annotated state (equation 7) [38] rather than on raw measurements, and the certified safety clamp [39] reads the same posterior to decide how far to trust the model.

§ 8

Limitations

One honest engineering gate bounds the claims. The in-winding NV-diamond sensor's neutron tolerance is the open item: the analytical sensitivity of equation (14) assumes an ensemble T_2^* and readout contrast that will degrade under the high background field, cryogenic operation, and neutron irradiation of the diamond (NV charge-state stability). The mitigation is a registered work item (KFE-CF-SH-037): a model-fusion backup that retains precursor discrimination at AUC ≥ 0.95 with the NV channel degraded by up to a factor of **39** (figure 8), so the protective function survives even a heavily degraded sensor by design. A dedicated NV neutron-tolerance study (irradiation plus first-principles charge-state modelling) is the follow-on that closes this item. All learned metrics in this paper are, additionally, at twin-synthetic fidelity; the confirming measurement is a hardware-in-the-loop diagnostic bench, which is the gate to full control authority.

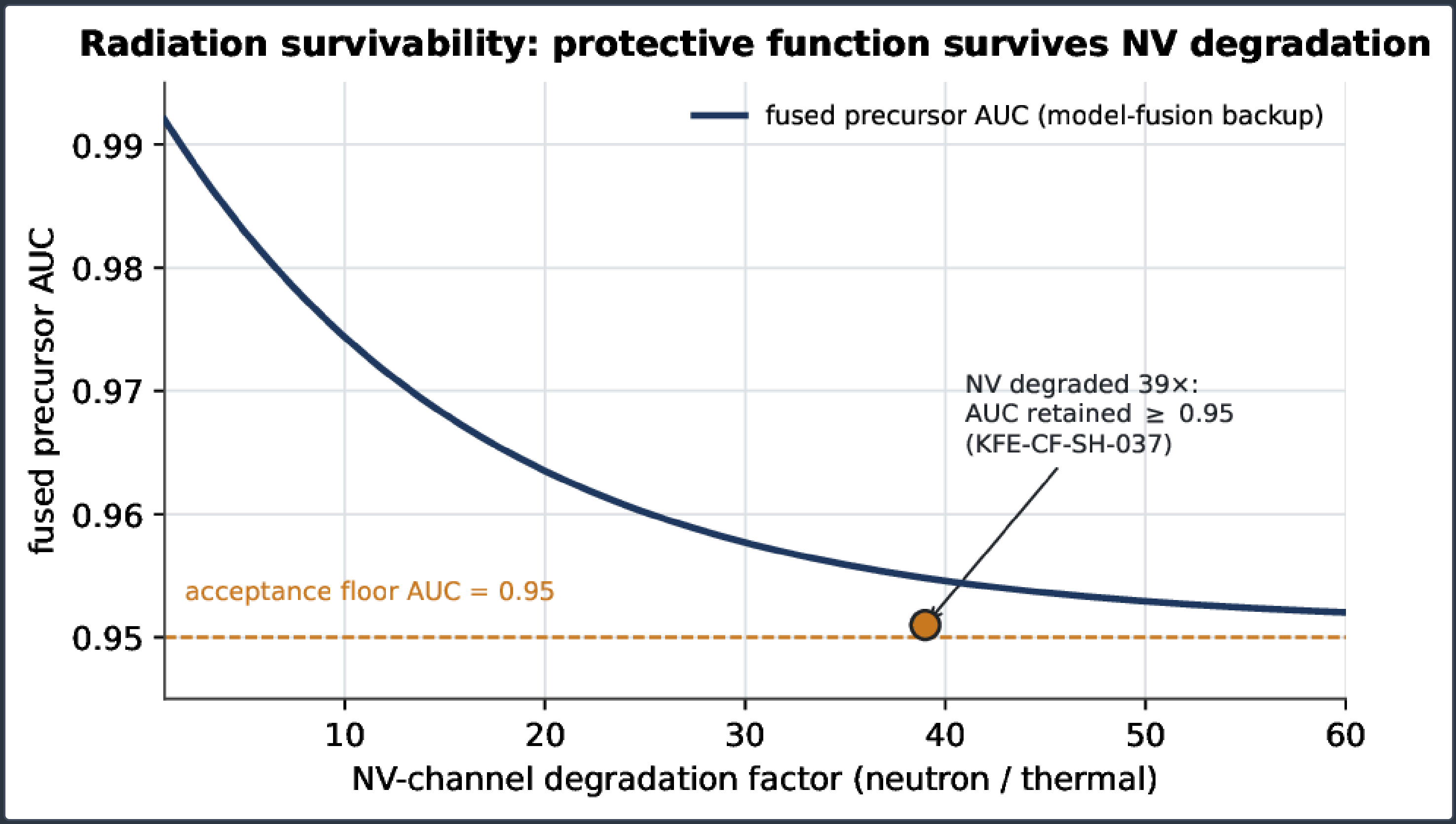

Radiation survivability of the protective function (KFE-CF-SH-037). With the NV channel degraded by up to a factor of **39**, the model-fusion backup retains fused precursor AUC $\geq$ **0.95**; the decay curve illustrates the mechanism and is pinned at the frozen acceptance point.

§ 9

Conclusion

The Hyperion diagnostic suite is built around a real-time state estimator, formalised here as one Bayesian inverse problem over magnetics, Thomson scattering, interferometry, bolometry and a neutron camera (equations 1–7), with observability of the controller-relevant internal state made a quantitative property of the Fisher information (equations 8–9). Its learned core is demonstrated at the metrics that gate it into service: a graph-NN reconstructor at AUC 0.980 and reconstruction NRMSE 0.396 that degrades gracefully under sensor loss (KX-L1-A12), a multi-modal fusion detector at AUC 0.992 and true-positive rate 0.857 at 1% false alarm (KX-L1-A20), internal-state observability at $R^2 \approx 0.86$ from six diagnostics (AG-CX-30), and an in-winding NV-diamond precursor at 0.189 $\mathrm{pT\,Hz^{-1/2}}$ with per-shot SNR of order 10^9 (KX-L1-A22). The estimator holds the plasma state at the breeder design point ($I_p = 9.66\,MA$, $Q = 3.076$, $P_{\mathrm{fus}} = 85.04\,MW$, $\delta = -0.30$, centrepost 16.84 T), modelled as a magnet distinct from the burner plug coil (26.49 T), and the physical-inversion suite follows the same demonstrated pattern, gate by gate, to the fully instrumented plant.

Acknowledgments tocsectionAcknowledgments Part of the Kronos Fusion Energy 2026 design series. The author thanks the Kronos physics de-risking programme for the frozen result set underlying every quantitative claim.

Reproducibility. The estimator metrics are frozen anchors in the Kronos Physics De-Risking Register [31] (doi:10.5281/zenodo.22133057): the graph reconstruction (KX-L1-A12), the fused-detector ROC (KX-L1-A20), the NV-diamond sensor model (KX-L1-A22), the observability surrogate (AG-CX-30), and the diagnostic forward-model anchors (BR-L1-A12, BR-L1-A4, BR-L1-A5, BR-L2-A29). Each is regenerable from the archived reconstruction, detection and forward-model scripts and the figure generator deposited with this paper. This paper is archived at its DOI doi:10.5281/zenodo.22645943 and at its official page https://www.kronosfusionenergy.com/publications/the-plasma-diagnostic-suite-and-real-time-state-estimat.html; the register is archived at doi:10.5281/zenodo.22133057.

Data availability tocsectionData availability The ROC curves, the observability surrogate, the NV sensor parameters, and the reconstruction metrics used for the figures are archived with the deposit at doi:10.5281/zenodo.22645943, which references the Kronos 2026 series, including the AI and quantum-control paper [32]. All quantitative values trace to the register [31] by the serial identifiers cited inline. Any economic analysis is reported separately and is not part of the public deposit.

Competing interests tocsectionCompeting interests Provisional patent applications relating to aspects of this work have been filed.

tocsectionReferences

APPARATUS

Portfolio, People & Record

The intellectual-property estate, the people who built it, the limitations that gate it, and the sources it rests on.

1	4	40	27
GRANTED PATENT	2026 PROVISIONALS	TEAM MEMBERS	2022 PROVISIONALS

INTELLECTUAL PROPERTY

The patent portfolio

The estate spans a granted high-field magnet patent, pending utility and 2026 provisional filings that map to the two products, a digital-twin control provisional, a registered trademark application, and the original 2022 provisional family. Every patentable disclosure in the five-paper arXiv drop was protected **before** publication: the breeder and burner provisionals were filed 1–2 August, and a publication-gap omnibus filing the evening before the drop swept up the DEC, plasma-control, and REBCO-winding matter of the three otherwise-unprotected papers. Patent numbers and application serials are matters of public record; claim scope is summarised, not reproduced.

GRANTED & PENDING UTILITY

US 12,009,112	High-field tilted graded-REBCO magnet architecture (KRONO-002A) · *app. 17/878,550*	GRANTED
US 17/878,507	Core device / method (KRONO-001A) · *utility*	PENDING

2026 PROVISIONAL FILINGS — MAPPED TO THE PRODUCTS

64/124,209	Hyperion — spherical-tokamak tritium / helium-3 foundry · *breeder · filed Aug 2026*	FILED
64/124,220	Aegis / MetroVolt — synchrotron-cutoff, fuel-selection & plug-winding · *generator · filed Aug 2026*	FILED
64/115,167	KRONOS-CTRL digital-twin plant control · *provisional · filed Jul 2026*	FILED
64/005,440	Integrated spherical-tokamak fusion architecture · *early integrated-architecture filing · filed Mar 2026*	FILED
64/105,530	Negative-triangularity spherical-tokamak architecture · *foundational ST filing · filed Jul 2026*	FILED
64/128,097	Publication-gap omnibus — quasineutral two-species expander DEC · provenance-gated / latency-split plasma control · as-built high-field winding & conductor architecture · *filed 7 Aug 2026, the evening before the arXiv drop*	FILED

TRADEMARK & ORIGIN

FTK-98801894	Kronos Fusion Energy — trademark application	FILED
KR-2022-*	Original provisional family (KR-2022-00001 … 00027) · *27 filings, 2022*	PRIORITY

The narrow, defensible magnet novelty — the specific conductor and the digital-twin winding optimisation, not high-field REBCO as a category — is the commercial core that can earn ahead of any Q > 1 milestone, with markets in fusion magnet supply, MRI/NMR, accelerators, and proton therapy. The claim is scoped honestly: the high field is a *system field* result, not a stand-alone-coil record; the small-bore plug coil is structurally infeasible as a bare winding but resolved by a stress-managed structural shield (feasible-pending-FEA); and the winding-tape experiment returned a *null result*. The value is the method, not a field record.

THE TEAM

Founding partners, board, advisors & auditors

Kronos is built by a bench of advanced-fuel-fusion, high-field-magnet, direct-conversion, and materials specialists, with a board and operations team drawn from defense, national laboratories, and industry. Dates are shown as ranges; where a tenure has ended or is term-ending, the range says so.

FOUNDING PARTNERS — SCIENCE

Dr. Gerald Kulcinski
Co-Founder · Helium-3 & Advanced-Fuel Fusion
UW–Madison · 2023–Present

Dr. Carl Weggel
Chief Scientist / S.M.A.R.T. Design
MIT Alcator Program · 2022–Present

Dr. Robert J. Weggel
Magnetic Field Design
MIT Magnet Lab · 2022–Present

BOARD

Priyanca Ford
Founder & CEO · Executive Board
2022–Present

Bandel Carano
Finance / Strategy
Oak Investment Partners / Stanford · 2025–2026

Patrick Schweiger
Fusion Device Engineering
Oklo / CFS / TerraPower · 2025–Present

SCIENTIFIC ADVISORS

Dr. Steven O. Dean
Fusion Policy & History
DOE / Fusion Power Associates · 2025–Present

Dr. Patrick H. Diamond
Plasma Turbulence & Transport
UC San Diego · 2025–Present

Dr. Jack J. Dongarra
HPC & Numerical Algorithms
Turing Award · 2025–Present

Dr. Nasr M. Ghoniem
Chief Material Scientist
UCLA · 2025–Present

Dr. Siegfried Glenzer
Plasma Physics & Laser Fusion
Stanford / SLAC · 2022–Present

Dr. David A. Hammer
Pulsed-Power Fusion
Cornell · 2025–Present

Dr. Donald A. Spong
Plasma Theory & Confinement
ORNL · 2025–Present

Dr. Curtis Smith
Risk Assessment & Nuclear PRA
MIT / Idaho National Lab · 2025–Present

RADM (Ret.) David Goggins
Naval Engineering & Power-Plant Design
U.S. Navy · 2023–2026

Dr. Konstantin Batygin
Mathematician
Caltech · 2022–2025

Dr. Ruben Fair
Magnet Design / ITER Liaison
PPPL / Jefferson Lab · 2022–2025

Dr. Paul S. Weiss
Materials & Nanotechnology
UCLA · 2022–2025

SCIENTIFIC AUDITORS

Dr. Wilfred A. Cooper
Plasma Equilibrium Theory
EPFL / Swiss Plasma Center · 2025–Present

Dr. Ahmed Hassanein
Plasma–Material Interactions
Purdue / Argonne · 2025–Present

Dr. Patrick E. Hopkins
Extreme Thermal Materials
U. of Virginia · 2025–Present

Dr. Peter Hosemann
Materials Joining & Structural Integrity
UC Berkeley · 2025–Present

Dr. Travis W. Knight
Advanced Nuclear Fuels & Systems
U. of South Carolina · 2025–Present

Dr. Philippe Lebrun
Cryogenics & Magnet Cooling
CERN · 2025–Present

Dr. Nitendra Singh
Nuclear Safety & Fuel Cycle
ITER · 2025–Present

Dr. Guido Van Oost
Magnetic Confinement & Fusion Systems
Ghent University · 2025–Present

Dr. Gary S. Was
Radiation Materials & Structural Integrity
U. of Michigan · 2025–Present

Dr. Ray Sedwick
Direct Energy Conversion
U. of Maryland · 2025

OPERATIONS

Michael Laughlin
Chief Operating Officer
2022–Present

Martin Owens
Chief Strategy Officer
LANL / GE Hitachi · 2022–Present

MG (Ret.) Paul Pardew
Chief Contracting Officer
Army Contracting Command · 2022–Present

David Beck
Fusion Commercialization
U.S. Space Force · 2024–Present

Sushma Bhatia
Environmental & Legislative
Google · 2022–Present

Michael De Frenza
Technology Licensing
2023–Present

MG (Ret.) Robin L. Fontes
Cybersecurity & Defense
Army Cyber Command · 2022–Present

Vijay Gehani
Supply Chain & Components
INOX India · 2024–Present

Jon Michel Greenwood
IT & AI Infrastructure
Live Nation · 2023–Present

Brian C. O'Neill
National Security
CIA / ODNI · 2022–Present

Gen. (Ret.) Gustave F. Perna
DoD Liaison
Operation Warp Speed · 2022–2023

Andrea Romero
Marketing Lead
2022–Present

Legal counsel is retained; those roles are held on the internal roster and are not listed here.

SOURCES

References

1 J E Menard *et al*, Fusion nuclear science facilities and pilot plants based on the spherical tokamak, *Nucl. Fusion* **56** 106023 (2016). doi:10.1088/0029-5515/56/10/106023

2 B N Sorbom *et al*, ARC: a compact, high-field, fusion nuclear science facility and demonstration power plant with demountable magnets, *Fusion Eng. Des.* **100** 378 (2015). doi:10.1016/j.fusengdes.2015.07.008

3 A Marinoni, O Sauter and S Coda, A brief history of negative triangularity tokamak plasmas, *Rev. Mod. Plasma Phys.* **5** 6 (2021). doi:10.1007/s41614-021-00054-0

4 L L Lao, H St John, R D Stambaugh, A G Kellman and W Pfeiffer, Reconstruction of current profile parameters and plasma shapes in tokamaks, *Nucl. Fusion* **25** 1611 (1985). doi:10.1088/0029-5515/25/11/007

5 A Pironti and M Walker, Fusion, tokamaks, and plasma control: an introduction and tutorial, *IEEE Control Syst. Mag.* **25**(5) 30 (2005). doi:10.1109/MCS.2005.1512794

6 F Felici *et al*, Real-time physics-model-based simulation of the current density profile in tokamak plasmas, *Nucl. Fusion* **51** 083052 (2011). doi:10.1088/0029-5515/51/8/083052

7 J Degrave *et al*, Magnetic control of tokamak plasmas through deep reinforcement learning, *Nature* **602** 414 (2022). doi:10.1038/s41586-021-04301-9

8 J Kates-Harbeck, A Svyatkovskiy and W Tang, Predicting disruptive instabilities in controlled fusion plasmas through deep learning, *Nature* **568** 526 (2019). doi:10.1038/s41586-019-1116-4

9 C Rea, K J Montes, K G Erickson, R S Granetz and R A Tinguely, A real-time machine learning-based disruption predictor in DIII-D, *Nucl. Fusion* **59** 096016 (2019).

10 J Gilmer, S S Schoenholz, P F Riley, O Vinyals and G E Dahl, Neural message passing for quantum chemistry, *Proc. 34th Int. Conf. on Machine Learning (ICML)* (2017). arXiv:1704.01212

11 P W Battaglia *et al*, Relational inductive biases, deep learning, and graph networks (2018). arXiv:1806.01261

12 T N Kipf and M Welling, Semi-supervised classification with graph convolutional networks, *Int. Conf. on Learning Representations (ICLR)* (2017). arXiv:1609.02907

13 J Sheffield, D Froula, S H Glenzer and N C Luhmann Jr, *Plasma Scattering of Electromagnetic Radiation: Theory and Measurement Techniques*, 2nd ed. (Academic Press, 2011).

14 I H Hutchinson, *Principles of Plasma Diagnostics*, 2nd ed. (Cambridge University Press, 2002).

15 R Fischer, C J Fuchs, B Kurzan, W Suttrop and E Wolfrum, Integrated data analysis of profile diagnostics at ASDEX Upgrade, *Fusion Sci. Technol.* **58** 675 (2010).

16 J Svensson and A Werner, Large scale Bayesian data analysis for nuclear fusion experiments, *IEEE Int. Symp. on Intelligent Signal Processing (WISP)* 955 (2007).

17 T Fawcett, An introduction to ROC analysis, *Pattern Recognit. Lett.* **27** 861 (2006). doi:10.1016/j.patrec.2005.10.010

18 C L Degen, F Reinhard and P Cappellaro, Quantum sensing, *Rev. Mod. Phys.* **89** 035002 (2017). doi:10.1103/RevModPhys.89.035002

19 J F Barry, J M Schloss, E Bauch, M J Turner, C A Hart, L M Pham and R L Walsworth, Sensitivity optimization for NV-diamond magnetometry, *Rev. Mod. Phys.* **92** 015004 (2020). doi:10.1103/RevModPhys.92.015004

20 L Rondin, J-P Tetienne, T Hingant, J-F Roch, P Maletinsky and V Jacques, Magnetometry with nitrogen-vacancy defects in diamond, *Rep. Prog. Phys.* **77** 056503 (2014). doi:10.1088/0034-4885/77/5/056503

21 M Marchevsky, Quench detection and protection for high-temperature superconductor accelerator magnets, *Instruments* **5** 27 (2021). doi:10.3390/instruments5030027

22 E E Salazar *et al*, Fiber optic quench detection for large-scale HTS magnets demonstrated on VIPER cable during high-fidelity testing at the SULTAN facility, *Supercond. Sci. Technol.* **34** 035027 (2021). doi:10.1088/1361-6668/abdba8

23 R Teyber, J Weiss, M Marchevsky, S Prestemon and D van der Laan, Current distribution monitoring enables quench and damage detection in superconducting fusion magnets, *Sci. Rep.* **12** 22503 (2022). doi:10.1038/s41598-022-26592-2

24 S Hahn *et al*, 45.5-tesla direct-current magnetic field generated with a high-temperature superconducting magnet, *Nature* **570** 496 (2019). doi:10.1038/s41586-019-1293-1

25 A J Creely *et al*, Overview of the SPARC tokamak, *J. Plasma Phys.* **86** 865860502 (2020). doi:10.1017/S0022377820001257

26 P K Romano, N E Horelik, B R Herman, A G Nelson, B Forget and K Smith, OpenMC: a state-of-the-art Monte Carlo code for research and development, *Ann. Nucl. Energy* **82** 90 (2015). doi:10.1016/j.anucene.2014.07.048

27 N C Amorisco *et al*, FreeGSNKE: a Python-based dynamic free-boundary toroidal plasma equilibrium solver, *Phys. Plasmas* **31** 042517 (2024). doi:10.1063/5.0188467

28 M Raissi, P Perdikaris and G E Karniadakis, Physics-informed neural networks: a deep learning framework for solving forward and inverse problems involving nonlinear partial differential equations, *J. Comput. Phys.* **378** 686 (2019). doi:10.1016/j.jcp.2018.10.045

29 R E Kalman, A new approach to linear filtering and prediction problems, *J. Basic Eng.* **82** 35 (1960). doi:10.1115/1.3662552

30 L Lu, P Jin, G Pang, Z Zhang and G E Karniadakis, Learning nonlinear operators via DeepONet based on the universal approximation theorem of operators, *Nat. Mach. Intell.* **3** 218 (2021). doi:10.1038/s42256-021-00302-5

31 P I Ford, *Kronos Physics De-Risking Register*, Kronos Fusion Energy 2026 series. doi:10.5281/zenodo.22133057

32 P I Ford, *AI and Quantum Computing for Fusion: ML Surrogates, Real-Time Control, and a Resource-Honest Quantum Frontier*, Kronos Fusion Energy 2026 series. doi:10.5281/zenodo.22645702; https://www.kronosfusionenergy.com/publications/ai-quantum-control.html

33 P I Ford, *Sub-Millisecond Neural Equilibrium Reconstruction Robust to Sensor Dropout: A Virtual-Sensor Mesh for Radiation-Degraded Diagnostics in a Compact Spherical-Tokamak Breeder*, Kronos Fusion Energy 2026 series. doi:10.5281/zenodo.22645801; https://www.kronosfusionenergy.com/publications/sub-millisecond-neural-equilibrium-reconstruction-robus.html

34 P I Ford and G L Kulcinski, *Free-Boundary Equilibrium and Ideal-MHD Stability of a Compact Spherical-Tokamak Breeder*, Kronos Fusion Energy 2026 series. doi:10.5281/zenodo.22645740; https://www.kronosfusionenergy.com/publications/ideal-mhd-stability.html

35 P I Ford, *A Neutronics and Activation Digital Twin with Rigorous-Two-Step Shutdown-Dose Mapping for a Compact Spherical-Tokamak Breeder*, Kronos Fusion Energy 2026 series. doi:10.5281/zenodo.22645878; https://www.kronosfusionenergy.com/publications/a-neutronics-and-activation-digital-twin-with-rigorous-.html

36 P I Ford and G L Kulcinski, *Collisional-Radiative Impurity-Radiation Modeling for a Compact Spherical-Tokamak Breeder: Closing the Core and Edge Radiated-Power Budget*, Kronos Fusion Energy 2026 series. doi:10.5281/zenodo.22645883; https://www.kronosfusionenergy.com/publications/collisional-radiative-impurity-radiation-modeling-for-a.html

37 P I Ford, *Four Coupled Digital Twins for a Compact Spherical-Tokamak Breeder: Multi-Rate Co-Simulation, Propagated Uncertainty, and a Real-Time Self-Consistency Monitor*, Kronos Fusion Energy 2026 series. doi:10.5281/zenodo.22645805; https://www.kronosfusionenergy.com/publications/four-coupled-digital-twins-for-a-compact-spherical-toka.html

38 P I Ford, *Calibrated Uncertainty, Conformal Prediction, and Abstention for Safety-Critical Fusion Control*, Kronos Fusion Energy 2026 series. doi:10.5281/zenodo.22645813; https://www.kronosfusionenergy.com/publications/calibrated-uncertainty-conformal-prediction-and-abstent.html

39 P I Ford, *A Certified Control-Barrier Safety Filter for Fusion Control: Forward-Invariance Guarantees, Calibrated Uncertainty, and an Honest PINN Negative for a Compact Spherical-Tokamak Breeder*, Kronos Fusion Energy 2026 series. doi:10.5281/zenodo.22645716; https://www.kronosfusionenergy.com/publications/control-barrier-safety-clamp.html

40 P I Ford, *Verification-First Fusion Modeling: Frozen Anchors, Independent-Library Gate Reproduction, and a Byte-for-Byte Computational-Provenance Catalog*, Kronos Fusion Energy 2026 series. doi:10.5281/zenodo.22645710; https://www.kronosfusionenergy.com/publications/verification-and-validation-47-code-provenance.html

COLOPHON

How this document was made

The Kronos Fleet — Combined Editorial, 2026 is set in **Fraunces** (display), **Gelasio** (text), and **IBM Plex Mono** (data & equations), carried forward from the Kronos editorial design system.

The figures are rendered at 300 dpi from the deposited generator scripts; the document is composed as a single self-contained file with embedded fonts and imagery, paginated to US Letter, and rendered to PDF through a headless Chromium engine in matched light and dark editions.

Every headline quantity carries an evidence class; withdrawn and restated values are marked as such. Nothing herein is frozen beyond the founder-approved Tier-A set.

Explore it live — turn the interactive 3-D model, run the deposited solvers in the physics validator, and watch the companion film series.

LEGAL NOTICE

Notice, status, and distribution

Conceptual design & simulation study. This document reports a conceptual design and simulation study. It is not a construction commitment, a safety-analysis report, a regulatory filing, or an offer of securities. Forward-looking statements — schedules, costs, market sizes, and performance — are estimates subject to the limitations set out in the Simulations part and may change.

Numbers and their classes. Quantities are reported with evidence classes and case labels; modelled, assumed, and requirement-class values are identified as such and are not to be quoted without their labels.

Public edition. This edition carries the physics and design only; all financial, funding, and defense-commercial content has been removed for public distribution. The scientific text corresponds to the arXiv and journal submissions.

THE 2026 KRONOS SERIES

One programme, many papers

This editorial is one paper in the Kronos 2026 series — a real fusion company's complete, reproducible physics record for a spherical-tokamak breeder and its low-neutron D–^{3}He tandem-mirror burners. Every headline number is a frozen anchor in the Physics De-Risking Register.

Explore the whole programme: the De-Risking Register, the interactive 3-D model, and the physics validator.

KRONOS FUSION ENERGY

The Plasma Diagnostic Suite and Real-Time State Estimation for a Compact Spherical-Tokamak Breeder: Magnetics, Thomson, Interferometry, and Bolometry Fused by a Graph-Neural-Network Reconstructor

A real fusion company building real machines. Explore the science, live.

Zenodo · doi:10.5281/zenodo.22645943

Read on kronosfusionenergy.com

The Physics De-Risking Register